Int. J. Electrochem. Sci., 15 **(2020)** 9168 – 9178, doi: 10.20964/2020.09.26

International Journal of
ELECTROCHEMICAL
SCIENCE
www.electrochemsci.org

New Synthesis route of Iron-Based Catalyst for Electrochemical Oxygen Reduction Reaction

Lu Qin[1], *Xiaochun Yu*[1], *Jun Li*[1,2,*], *Shuangyan Li*[1], *Yiyan Liu*[1], *Pengcheng Qian*[1], *Jichang Wang*[2,*], *Shun Wang*[1], *Huile Jin*[1,*]

[1] Nano-materials & Chemistry Key Laboratory, Institute of New Materials and Industrial Technologies, Wenzhou University, Wenzhou 325035, P. R. China.
[2] Department of Chemistry and Biochemistry, University of Windsor, Windsor, ON, N9B 3P4, Canada.
[*]E-mail: huilejin@wzu.edu.cn, junli@uwindsor.ca, jwang@uwindsor.ca

Received: 23 March 2020 / *Accepted:* 16 May 2020 / *Published:* 10 August 2020

Among existed oxygen reduction electrocatalysts, iron-based catalysts have shown great advantages of low cost and extraordinary reactivity, which are even comparable to commercialized platinum based catalysts. However, the propensity of iron catalysts to aggregate and passivate has emerged as a fundamental barrier to high-power fuel cell applications. In this study, biomass egg yolk derived carbon nanotubes were designed as an armor to host iron complexes, offering multiple active sites such as Fe-N_x, Fe_3C, Fe_2P for efficient oxygen reduction reaction (ORR). Although the true active sites of iron-based catalysts on the enhanced ORR activities is still under debates, a consensus on the contributions of Fe-N_x active center has been reached via a smart material design in this work, which enables ORR onset potential at 0.9 V vs. RHE with excellent four-electron selectivity in alkaline media. Meanwhile, the state-of-the-art carbon shells promote the performance stability remarkably (retaining above 96% of its activity after 27 hours).

Keywords: biomass derived, heteroatom doped carbon, supercapacitors, cycling stability, manganese dioxide

1. INTRODUCTION

An urgent demand for scaling up commercialized fuel cell systems is to replace the conventional platinum based catalysts with inexpensive and more reliable electrode materials[1-4]. Apart from their high price that is worth more than 50% of the fuel cell system cost[5-7], traditional platinum-based materials also suffer from high methanol crossover and severe carbon monoxide poisoning, which may result in structural instabilities and short lifetime[8-10]. Consequently, the replacement of platinum catalysts has become a hot and frontier research in materials science[11-13]. Tremendous efforts have

been devoted to fabricating new electrode materials[14], among which, iron is one of the very promising candidates because of its better oxygen reduction reaction (ORR) performance than most of the other transition metals (Fe > Co > Zn > Mn > Cu > Ni)[3, 15-18]. In addition, the carbon supports of Fe complexes can be produced in a sustainable way by utilizing biomass to prepare the carbon, provide part of the reactive sites, and build promising transport properties of ORR-relevant species[19]. Significantly, properties of the carbon backbone can be further tailored by intrinsic heteroatom doping and forming porous structure[8, 12, 20, 21]. However, it is still challenging to apply iron-containing carbon catalysts in practical applications[22], partially owing to the lack of understanding of iron active sites towards ORR and a strategy to sustain their activity and durability[17, 23-25].

In recent studies, iron coordinated with nitrogen atoms ($Fe–N_x$) has been recognized as an active center responsible for the excellent ORR catalytic performance[26-29]. Single atom experiments further demonstrate that a single iron atom incorporated with nitrogen can significantly improve the electron transfers from iron to the adsorbed hydroxyl radicals, making the rate determined step of charging the adsorbed hydroxyl radicals to hydroxide species more favorable[17]. However, as more iron-based active species are discovered via experimental and theoretical approaches, such as iron carbides (Fe-C), iron phosphides (Fe-P), iron sulfides (Fe-S), etc.[13, 19, 26, 30, 31], a heated and highly polarized debate about the true ORR active center has been raised. Recently, the $Fe–N_x$ complexes have been further proposed to be more active at acidic conditions, whereas other iron complexes are more active in alkaline media[8]. Moreover, even metal-free heteroatom-doped carbon exhibits promising pH-universal catalytic properties for oxygen reduction reaction[10, 32].

In order to shed light on the debates mentioned above, a smart material design strategy has been developed in this work by constructing different types of iron complexes in a novel carbon host for comparison purposes. To be more specific, a biomass candidate, chicken egg, has been selected as the precursor of carbon hosts, which also composed of rich phosphorus, nitrogen, and other elements[33], making the synthesis of multiple iron-active species feasible. Specifically, egg yolk and potassium ferricyanide are used as the starting materials to produce iron complexes. The as-prepared catalyst is denoted as egg yolk-derived carbon encapsulated iron complexes (Fe@EY-N_2), where N_2 indicates the thermal treatment being performed in nitrogen atmosphere. The additional thermal treatments towards Fe@EY-N_2 under NH_3 atmosphere successfully led to the reduction of iron oxides and the appearance of new phase Fe-N_x in the catalysts, named as Fe@EY-NH_3. Intriguingly, Fe@EY-NH_3 catalysts that contain Fe-N_x species show overwhelmingly better ORR performance compared to Fe@EY-N_2. The results suggest that in the prepared catalysts Fe-N_x species are likely the active sites and are more active than Fe_3C and Fe_2P.

2. EXPERIMENTAL

2.1. Chemicals

Fresh chicken eggs were purchased from local markets, potassium ferricyanide was purchased from Tianjin Guangfu Technology Development. All other reagents were purchased from Aladdin Reagent (Shanghai, P. R. China), such as potassium hydroxide, Nafion solution (5 wt%), commercial platinum carbon, methanol, etc.

2.2. Material preparation

In brief, the mass ratio of egg yolks and potassium ferricyanide was set as 1:5, where the actual mass of dried egg yolks and potassium ferricyanide is 3.5 g and 17.5 g, respectively. Both chemicals were dispersed in 60 mL deionized water and ultrasonicated for 30 min. After another 30 min vigorous hand stirring, the mixture was then transferred in an oven and reacted at 120 ℃ for 16 h. The raw products were then annealed under nitrogen atmosphere at 1000 ℃ for 2 h with a heating rate of 5 ℃ min^{-1}, the products were designated as Fe@EY-N_2. Further thermal treatments under NH_3 atmosphere at 1000 ℃ for 2 h with a heating rate of 5 ℃ min^{-1} were conducted to produce another form of catalysts denoted as Fe@EY-NH_3. As a control experiment, the same procedures were also conducted in the absence of potassium ferricyanide to produce pure egg yolk derived carbon catalysts, denoted as EY-NH_3. Salt can denature proteins in the same way heat does. Potassium may speed up the process of protein decomposition in egg yolk, which is facilitating the formation of carbon nanotube structures.

2.3. Characterizations

The as-obtained catalysts were characterized by scanning electron microscopy (SEM, Nova NanoSEM 200) operated at an acceleration voltage of 10 kV, transmission electron microscopy (TEM, JEM-2100, JEOL) and energy-dispersive X-ray spectroscopy that was taken during the TEM measurements. X-ray diffraction pattern (XRD, Bruker D8) was recorded by using Cu Kα radiation (λ = 0.15406 nm), and Raman spectroscopy (JY-T643200, France) was conducted at ambient temperature using a laser excitation of 514 nm. X-ray photoelectron spectroscopy (XPS) was performed on a spectrometer from Kratos Axis Ultradld, using Mono Al Kα radiation at a power of 120 W (8 mA, 15 kV). The nitrogen adsorption/desorption data were recorded at the liquid nitrogen temperature (77 K) using a micrometrics apparatus (ASAP 2020 M). The specific surface area was calculated using the BET equation.

2.4. Electrode preparation

6.0 mg of the as-prepared materials were mixed with ethanol (0.2 mL), de-ionized water (0.8 mL) and Nafion (5 wt%, 12 μL). The mixture was dispersed by ultrasonication for 1 h to achieve homogeneity. Subsequently, certain amount of catalyst ink was carefully coated on a glassy carbon electrode (5.0 mm in diameter) and dried in air for more than 12 h. The procedure led to a mass loading of about 0.8 mg cm^{-2}.

2.5. Electrochemical measurements

The electrochemical measurements were conducted at room temperature (25 ℃) on an Autolab electrochemical workstation. Three-electrode configurations were applied with the as-prepared catalysts, platinum and Ag/AgCl as working, counter and reference electrode, respectively. The ORR performance was evaluated by cyclic voltammetry (CV), linear sweep voltammetry (LSV) and chronoamperometric current-time (i-t curve) methods on a rotating disk electrode in O_2/Ar-saturated 0.1 M KOH. Methanol crossover tests were carried out by chronoamperometric technique at the applied potential of -0.20 V

(vs. RHE) in O_2-saturated 0.1 M KOH electrolytes with a rotation rate of 1600 rpm. Electrochemical impedance spectroscopy (EIS) tests were conducted in a frequency range of 100 kHz to 100 mHz with the perturbation amplitude of 10 mV.

3. RESULTS AND DISCUSSION

As shown in Figure 1, the as-obtained Fe@EY-NH_3 catalysts are composed of segmented iron complexes with a nanorod shape and carbon walled nanotubes (CNTs) with an average diameter of 100 nm, in which iron complexes are well confined within CNTs. The results confirm that iron complexes have been successfully generated and wrapped by egg yolk derived carbon shells via this in-situ encapsulation approach. Further characterization by high-angle annular dark-field scanning transmission electron microscopy (HAADF-STEM) reveals that Fe@EY-NH_3 catalysts possess a uniform elemental distribution of C, O, Fe, N and P. However, the variation of chemical compositions for the N_2 calcined Fe@EY-N_2 and NH_3 activated Fe@EY-NH_3 catalysts is not obvious according to the elemental analysis. Furthermore, it is worth noting that the nanotube structure is quite sensitive to the calcination temperatures, which can be only generated beyond 1000 ℃. Random clusters were formed at 900 ℃, while 1100 ℃ is too high to maintain the integrity of the nanotube structure.

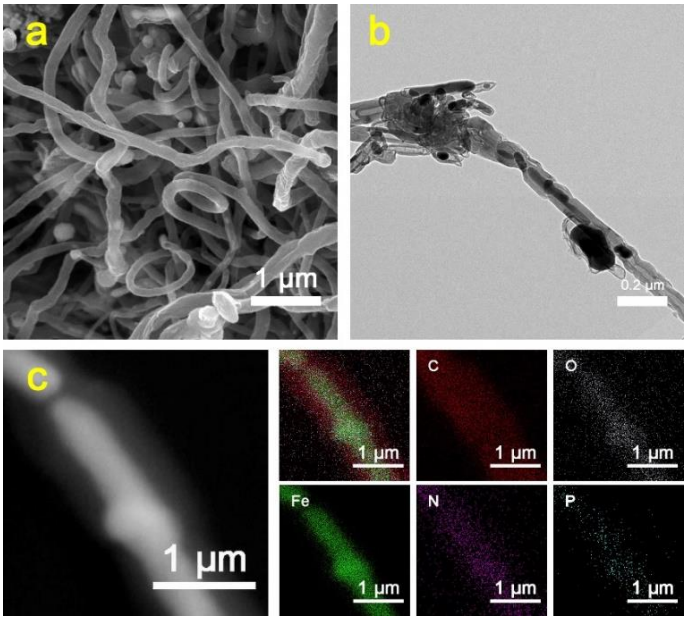

Figure 1. (a) SEM images of the Fe@EY-NH_3; (b) TEM image of the Fe@EY-NH_3; (c) the EDS elemental distributions of Fe@EY-NH_3.

Interestingly, the X-ray photoelectron spectrum was able to illustrate more detailed subtle variations. These measurements show that the additional thermal treatments towards Fe@EY-N_2 under NH_3 atmosphere successfully led to the formation of new Fe-N_x phase evidenced by the peak of 399.6 eV in Figure 2b and the peak of 713.3 eV in Figure 2c. Besides, NH_3 calcination process also significantly influence the state of oxidized-N 404.8 eV by the reduction of oxidized-N species. Notably,

other active iron species such as Fe_3C and Fe_2P potentially promoting ORR activities are both found in Fe@EY-N_2 and Fe@EY-NH_3 catalysts. The binding energy at 711.4 eV and 728.9/732.8 eV corresponds to the formation of carbonized or oxidized iron, which is in good agreement of O 1s and C 1s spectra. Meanwhile, the binding energy at 709.9 eV and 723.3 eV should be an indicator of Fe_2P. In this scenario, the appeared Fe_2O_3 and Pe_2P phases in Fe@EY-N_2 catalysts are significantly diminished due to the reduction of iron oxides by NH_3 at high temperatures (as shown in Figure 2e). The diverse active iron species in both forms of catalysts may endow a great opportunity on verifying the exact active center for ORR activities. To be more specific, Fe-N_x is a newly generated phase in Fe@EY-NH_3 compared to Fe@EY-N_2, making suitable active species for addressing research debates of true active center in this domain.

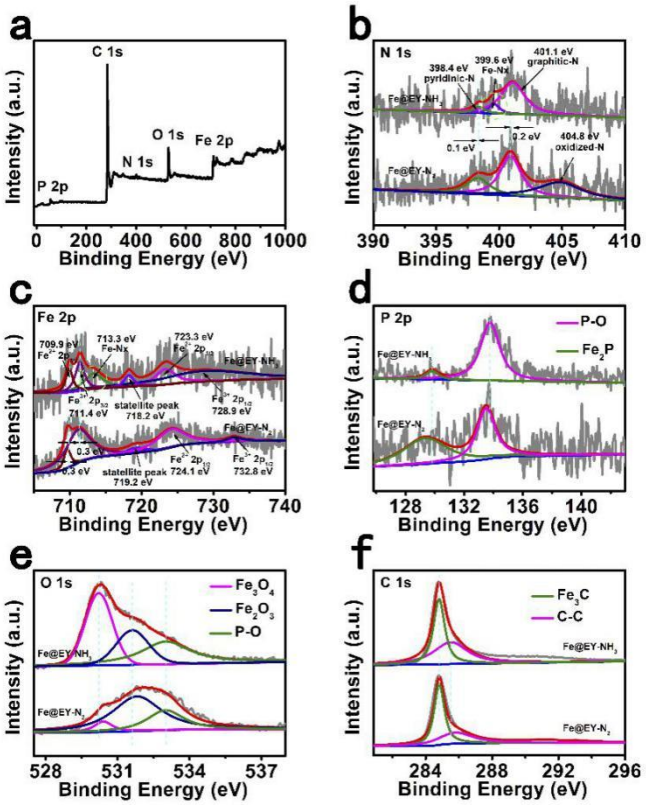

Figure 2. XPS spectra of the Fe@EY-NH_3 catalysts, (a) survey spectrum; (b) N 1s; (c) Fe 2p; (d) P 2p; (e) O 1s; (f) C 1s.

X-ray diffraction (XRD) was performed to further uncover the phase composition of those possible ORR active centers. As shown in Figure 3a, pure egg yolk derived carbon only exhibits two broad peaks centered at 26.3° and 43.8°, corresponding to the (002) and (100) planes of graphite, respectively. The introduction of iron complexes in the Fe@EY-N_2 and Fe@EY-NH_3 catalysts overwhelm the carbon signals, both exhibiting Fe_3C and Fe_2P phases in general. Comparing to the Fe@EY-N_2 catalysts, a new phase of Fe-N_x arises at around 40° in the Fe@EY-NH_3 catalysts, which is consistent with the XPS results. Indeed, the formation of Fe-N_x in iron-based catalysts via a second heat

treatment in NH_3 is a well-known strategy, allowing oxidized iron species to be drastically reduced by NH_3 and doped with nitrogen. The structure defect is supported by Raman spectra, in which a disorder-induced D band and in-plane vibrational G band clearly demonstrate the existence of defected and graphitic carbon. A high I_D/I_G ratio of Fe@EY-NH_3 suggests that numerous defects are induced by heteroatom doping in the catalysts, which are favorable for the electrochemical catalysis. The calculated Brunauer–Emmett–Teller (BET) value suggests that the introduction of iron complexes results in the deterioration of specific surface area of Fe@EY-NH_3 (9.65 $m^2 g^{-1}$), when being compared to the pure carbon generated from egg yolk (24.51 $m^2 g^{-1}$).

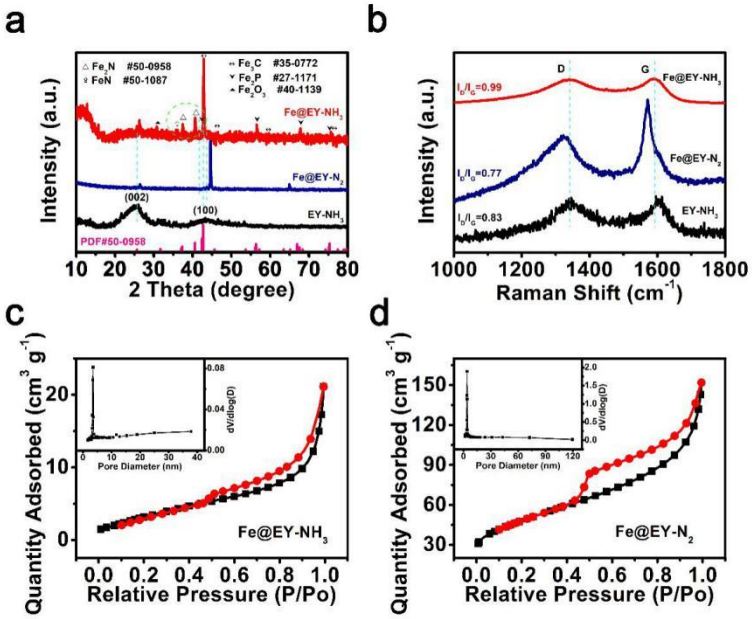

Figure 3. (a) XRD patterns of Fe@EY-NH_3, Fe@EY-N_2 and EY-NH_3; (b) Raman spectra of Fe@EY-NH_3 and EY-NH_3; (c,d) N_2 adsorption/desorption isotherms and the corresponding pore-size distribution curves (insets) of Fe@EY-NH_3 and Fe@EY-N_2.

In order to discriminate the role of different catalytic sites on the observed catalytic activity and gain further insights on the iron-based active center for the ORR, pure egg yolk derived carbon, Fe@EY-N_2 and Fe@EY-NH_3 catalysts are evaluated respectively by cyclic voltammetry (CV) and linear sweep voltammetry (LSV) in Figure 4. In the absence of iron complexes, carbon catalysts derived from pure egg yolk (i.e., EY-NH_3) exhibits barely any ORR signals. In a similar scenario, Fe@EY-N_2 catalysts that are dominated by Fe_3C and Fe_2P species show very weak ORR activities. However, a pronounced reduction peak is occurred at around 0.8 V (vs. RHE) with a positive onset potential of 0.9 V (vs. RHE) using Fe@EY-NH_3 catalysts, which is even comparable to the 20 wt% commercial Pt/C catalysts. Such significant improvement shall be attributed to the presence of Fe-N_x in the Fe@EY-NH_3 catalysts.

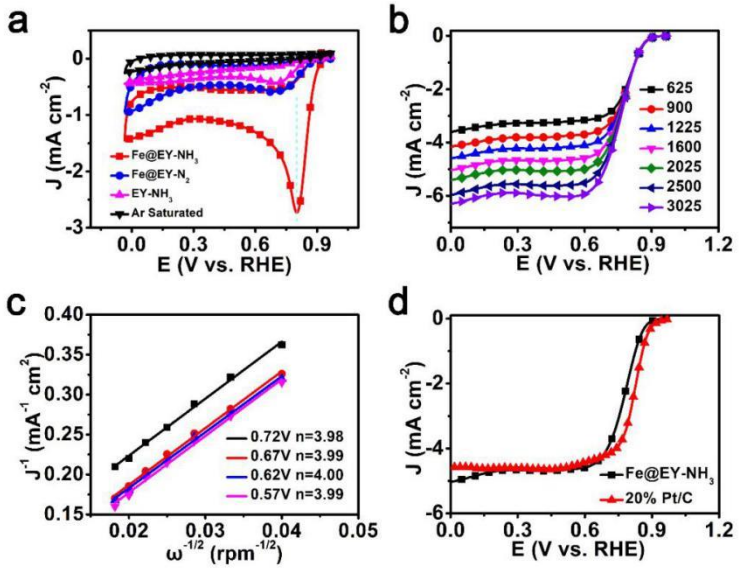

Figure 4. (a) Cyclic voltammetry curves of Fe@EY-NH_3 in Ar-saturated or O_2-saturated 0.1 M KOH; (b) LSV of O_2-saturated 0.1 M KOH solution at working electrodes prepared with different electrocatalysts at a disk rotating rate of 1600 rpm and a scanning rate of 10 mV s^{-1}; (c) K-L plots at various potentials; (d) RDE voltammograms (1600 rpm rotation speed) for the typical Fe@EY-NH_3 catalyst and 20% Pt/C.

The above control experiments strongly support that for the ORR in alkaline media the key reactive center in iron-containing carbon catalysts would be Fe-N_x, rather than Fe_3C, Fe_2P or heteroatom-doped carbon. In addition, iron atom in Fe-N_x could be coordinated by pyridinic N as seen in Figure 2b, which contributes to different properties and hence lead to excellent ORR activities. The further discrimination of the effective type of Fe-N_x will need more work to identify and quantify the fine structure of Fe-N_x and their neighboring carbon structures via more state-of-the-art techniques[34-36]. The Koutechy-Levich (K-L) analysis was applied to understand the charge transfer mechanism derived from ORR kinetics at different rotating rates of the rotating disk electrode (RDE) coated with the prepared catalysts. The corresponding K-L plots in Figure 4c clearly display the ORR electron transfer numbers (n=4), indicating a standard four electron transfer pathway.

The percentage of H_2O_2 yield was obtained by using a rotating-ring disk electrode (RRDE), As can be seen over the potential range of 0-0.8 V (vs. RHE) in Figure 5b, less than 5% of H_2O_2 can be produced at Fe@EY-NH_3 electrode. Moreover, a better methanol tolerance and durability (retaining above 96% of its activity after 27 h) can be found in Figure 5c and 5d, compared to that of 20 wt% commercial Pt/C catalysts. Our characterization indicates that calcination under NH_3 contributes to the formation of true active center Fe-N_x, as other iron complexes without the presence of Fe-N_x lead to poor ORR activities, and egg yolk derived pure carbon catalysts demonstrate similar poor ORR performance, indicating Fe-N_x is an true active center in this work.

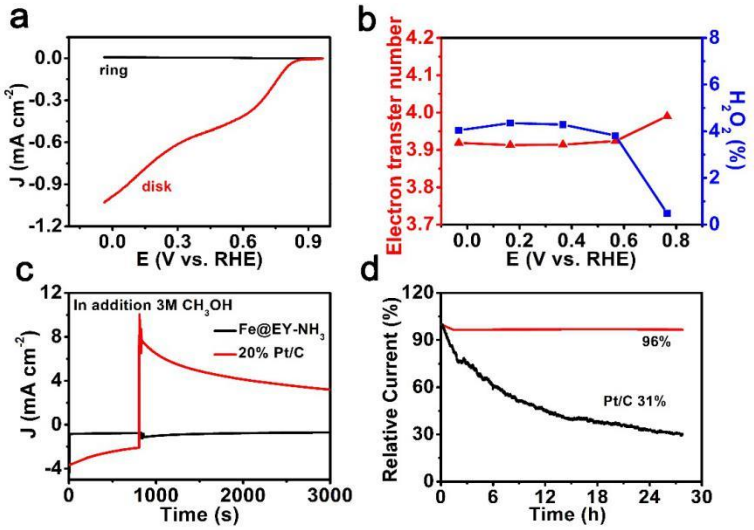

Figure 5. (a) RRDE voltammograms of the Fe@EY-NH_3 for ORR in O_2-saturated at a scan rate of 10 mV s^{-1}; (b) H_2O_2 yield and electron transfer number of Fe@EY-NH_3 obtained from RRDE measurement; (c) Current-time (i-t) chronoamperometric response of Fe@EY-NH_3 electrode at -0.20 V O_2-saturated 0.1 M KOH solution with a rotation rate of 1600 rpm; (d) Current-time (i-t) chronoamperometric response of Fe@EY-NH_3 and 20% Pt/C electrodes kept at -0.26 V in O_2-saturated 0.1 M KOH solution with a rotation rate of 1600 rpm.

To compare the ORR activities between this study and other similar Fe-N_x based electrocatalysts in the literature[37-49], the results are shown in Table 1. It is found that Fe-N_x based electrocatalyst in this study shows better ORR activities due to both high onset potential and half-wave potential, indicating Fe-N_x species plays a key role in ORR catalysts.

To be more specific, versatile strategies have been designed for the construction of Fe-N_x based catalysts, such as acid-leaching, heat treatments, the use of biomass in this work, and so on. Regardless what kinds of methods have been applied, the key factor is how to incorporate carbon with the active Fe-N_x sites. Recently, it was found that the kinetic activity of active Fe-N_x sites can be tuned by nitrogen functionalities in the carbon basal plane[39, 42-44]. More importantly, ORR intermediates are demonstrated to be adsorbed strongly on Fe-N_x sites[47], due to the delocalized π-band electrons in the carbon plane can interact with the d-orbital electrons in iron atom on Fe−N_x sites. However, if Fe-N_x sites were not appropriately incorporated with carbon, such as Fe@FeN_x[46] without carbon, ORR activity would be severely impeded by increasing the ORR intermediate adsorption energy. Meanwhile, carbon materials encapsulated Fe-N_x sites further improve the electrical conductivity and stability of the catalysts, such as metal-organic frameworks (MOF) encapsulated Fe-N_x sites [48] exhibited comparable ORR activities with CNT encapsulated Fe-N_x sites in this work.

Table 1. Comparison of ORR activities between Fe@EY-NH_3 and other Fe-N_x based catalysts from literature.

References	Materials	Onset potential (V vs. RHE)	Half-wave potential (V vs. RHE)
[37]	Fe-N-Carbon Black	0.849	0.746
[38]	Fe-Co-N-C	0.9	0.76
[39]	Fe-Nx/C	0.93	0.78
[40]	FePhcy	0.88	0.79
[41]	Fe/N/CHNSs-750	0.87	0.71
[42]	Fe–Nx/C	0.83	0.75
[43]	Pyrolyzed Fe-Nx/C	0.89	0.8
[44]	Fe-NxC	0.82	0.75
[45]	FeNx/carbon	0.89	0.8
[46]	Fe@FeNx	0.85	0.75
[47]	FeNC	0.9	0.78
[48]	Fe-N-C	0.9	0.8
[49]	EDTAFeNa-AL	0.89	0.75
This work	**Fe@EY-NH_3**	**0.9**	**0.81**

4. CONCLUSION

This study demonstrates a facile and effective strategy to construct carbon supported iron catalysts for the ORR. Together with the XPS and XRD measurements, our electrochemical experiments suggest that the existence of Fe-N_x species in the iron containing carbon can drastically boost its ORR catalytic activity and stability, even surpassing the benchmarks of commercial Pt/C catalysts. Notably, in the catalysts synthesized in this study other active sites such as Fe_3C, Fe_2P and heteroatom-doped carbon show poor ORR activities and appear to be less promising than the Fe-N_x active sites in alkaline media. Moreover, the assembled iron complexes encapsulated by CNTs endow the catalysts a long and stable cycle life, which is an appealing property for fuel cell applications.

ACKNOWLEDGEMENTS
This work was supported by the National Natural Science Foundation of China (51872209 and 51972239), the Wenzhou City Science and Technology Plan Project (No.2018ZG005 and W20170003) and Natural Sciences and Engineering Research Council of Canada (NSERC).

References

1. J. Mahmood, F. Li, C. Kim, H. J. Choi, O. Gwon, S. M. Jung, J. M. Seo, S. J. Cho, Y. W. Ju, H.Y. Jeong, G. Kim, and J.-B. Baek, *Nano Energy*, 44 (2018) 304.
2. Z. Wen, S. Ci, F. Zhang, X. Feng, S. Cui, S. Mao, S. Luo, Z. He, and J. Chen, *Adv. Mater.*, 24 (2012) 1399.
3. Z. Zhang, J. Sun, F. Wang, and L. Dai, *Angew. Chem., Int. Ed.*, 57 (2018) 9038.
4. K. Kumar, L. Dubau, M. Mermoux, J. Li, A. Zitolo, J. Nelayah, F. Jaouen, and F. Maillard, *Angew. Chem., Int. Ed.*, 59 (2020) 3235.
5. G. Wu, K. L. More, C. M. Johnston, and P. Zelenay, *Science*, 332 (2011) 443.
6. D. Sebastian, A. Serov, I. Matanovic, K. Artyushkova, P. Atanassov, A. S. Arico, and V. Baglio, *Nano Energy*, 34 (2017) 195.
7. L. Gidi, C. Canales, M. J. Aguirre, F. Armijo, G. Ramirez, *Int. J. Electrochem. Sci.*, 13 (2018) 1666.
8. M. Borghei, J. Lehtonen, L. Liu, and O. J. Rojas, *Adv. Mater.*, 30 (2018) 1703691.
9. H. Shen, T. Thomas, S. A. Rasaki, A. Saad, C. Hu, J. Wang, and M. Yang, *Electrochem. Energy Rev.*, 2 (2019) 252.
10. C. Yang, H. Jin, C. Cui, J. Li, J. Wang, K. Amine, J. Lu, and S. Wang, *Nano Energy*, 54 (2018) 192.
11. H. Lu, C. Yang, J. Chen, J. Li, H. Jin, J. Wang, and S. Wang, *Small*, (2020) DOI: 10.1002/smll.201906584.
12. L. Liu, X. Yang, N. Ma, H. Liu, Y. Xia, C. Chen, D. Yang, and X. Yao, *Small*, 12 (2016) 1295.
13. Z. Ma, S. Dou, A. Shen, L. Tao, L. Dai, and S. Wang, *Angew. Chem., Int. Ed.*, 54 (2015) 1888.
14. C. Z. Zhu, H. Li, S. F. Fu, D. Du, and Y. H. Lin, *Chem. Soc. Rev.*, 45 (2016) 517.
15. R. Ramachandran, S. M. Chen, G. P. G. Kumar, *Int. J. Electrochem. Sci.*, 10 (2015) 8581.
16. B. P. Vinayan, T. Diemant, R. J. Behm, and S. Ramaprabhu, *RSC Advances*, 5 (2015) 66494.
17. Y. Chen, S. Ji, Y. Wang, J. Dong, W. Chen, Z. Li, R. Shen, L. Zheng, Z. Zhuang, D. Wang, and Y. Li, *Angew. Chem., Int. Ed.*, 56 (2017) 6937.
18. H. J. Zhang, Q. Z. Jiang, L. Sun, X. Yuan, Z. Shao, and Z. F. Ma, *Int. J. Hydrogen Energy*, 35 (2010) 8295.
19. M. Xiao, J. Zhu, L. Feng, C. Liu, and W. Xing, *Adv. Mater.*, 27 (2015) 2521.
20. R. Paul, Q. B. Dai, C. G. Hu, and L. Dai, *Carbon Energy*, 1 (2019) 19.
21. P. Kaur, G. Verma, and S. S. Sekhon, *Prog. Mater. Sci.*, 102 (2019) 1.
22. G. A. Ferrero, K. Preuss, A. Marinovic, A. B. Jorge, N. Mansor, D. J. Brett, A. B. Fuertes, M. Sevilla, and M. M. Titirici, *ACS Nano*, 10 (2016) 5922.
23. R. Cao, R. Thapa, H. Kim, X. Xu, M. Gyu Kim, Q. Li, N. Park, M. Liu, and J. Cho, *Nat. Commun.*, 4 (2013) 2076.
24. M. Wang, Y. Yang, X. Liu, Z. Pu, Z. Kou, P. Zhu, and S. Mu, *Nanoscale*, 9 (2017) 7641.
25. D. Deng, L. Yu, X. Chen, G. Wang, L. Jin, X. Pan, J. Deng, G. Sun, and X. Bao*, Angew. Chem., Int. Ed.*, 52 (2013) 371.
26. S. Zhang, H. Zhang, W. Zhang, X. Yuan, S. Chen, and Z. F. Ma, *Chinese J. Catal.*, 39 (2018) 1427.
27. P. Zhao, X. Hua, W. Xu, W. Luo, S. Chen, and G. Cheng, *Catal. Sci. Technol.*, 6 (2016) 6365.
28. Y. Liu, Y. Zhu, H. Jiang, J. Shen, and C. Li, *Chem. Asian J.*, 15 (2020) 310.
29. G. Ren, L. Gao, C. Teng, Y. Li, H. Yang, J. Shui, X. Lu, Y. Zhu, and L. Dai, *ACS Appl. Mater. Interfaces*, 10 (2018) 10778.
30. Z. Y. Wu, X. X. Xu, B. C. Hu, H. W. Liang, Y. Lin, L. F. Chen, and S. H. Yu, *Angew. Chem., Int. Ed.*, 54 (2015) 8179.
31. J. Zhu, M. Xiao, G. Li, S. Li, J. Zhang, G. Liu, L. Ma, T. Wu, J. Lu, A. Yu, D. Su, H. Jin, S. Wang, and Z. Chen, *Adv. Energy, Mater.*, 10 (2020) 1903003.
32. L. Liu, G. Zeng, J. Chen, L. Bi, L. Dai, and Z. Wen, *Nano Energy*, 49 (2018) 393.
33. J. Zhang, H. Zhao, J. Li, H. Jin, X. Yu, Y. Lei, and S. Wang, *Adv. Energy Mater.*, 9 (2019) 1803221.

34. S. Choi, C. Kim, J. M. Suh, and H. W. Jang, *Carbon Energy*, 1 (2019) 85.
35. Y. Sun, X. Liu, Y. Jiang, J. Li, J. Ding, W. Hu, and C. Zhong, *J. Mater. Chem. A*, 7 (2019) 18183.
36. Y. Yuan, and J. Lu, *Carbon Energy*, 1 (2019) 8.
37. Y. Zhu, B. Zhang, D. Wang, D. Su, *ChemSusChem*, 8 (2015) 4016.
38. L. Osmieri, C. Zafferoni, L. Wang, A.H.A. Monteverde Videla, A. Lavacchi, S. Specchia, *ChemElectroChem*, 5 (2018) 1954.
39. Y. Wu, S. Zhao, K. Zhao, T. Tu, J. Zheng, J. Chen, H. Zhou, D. Chen, S. Li, *J. Power Sources*, 311 (2016) 137.
40. F. J. Perez-Alonso, C. Dominguez, S. A. Al-Thabaiti, A. O. Al-Youbi, M. A. Salam, A. A. Alshehri, M. Retuerto, M. A. Pena, S. Rojas, *J. Power Sources*, 327 (2016) 204.
41. D. Zhou, L. Yang, L. Yu, J. Kong, X. Yao, W. Liu, Z. Xu, X. Lu, *Nanoscale*, 00 (2014) 1.
42. A. V. Palenzuela, L. Zhang, L. Wang, P. L. Cabot, E. Brillas, K. Tsay, J. Zhang, *Electrochim. Acta*, 56 (2011) 4744.
43. L. Gao, M. Xiao, Z. Jin, C. Liu, J. Zhu, J. Ge, W. Xing, *J. Energy Chem.*, 27 (2018) 1668.
44. U. Tylus, Q. Jia, H. Hafiz, R. J. Allen, B. Barbiellini, A. Bansil, S. Mukerjee, *Appl. Catal. B: Environ.*, 198 (2016) 318.
45. J. Ding, P. Wang, S. Ji, H. Wang, V. Linkov, R. Wang, *Electrochim. Acta*, 296 (2019) 653.
46. Y. Chen, Z. Shi, Z. Wang, C. Wang, J. Feng, B. Pang, Q. Sun, L. Yu, L. Dong, *J. Alloys Comp.*, 829 (2020) 154558.
47. Y. Mun, S. Lee, K. Kim, S. Kim, S. Lee, J. W. Han, J. Lee, *J. Am. Chem. Soc.*, 141 (2019) 6254.
48. M. Xiao, J. Zhu, L. Ma, Z. Jin, J. Ge, X. Deng, Y. Hou, Q. He, J. Li, Q. Jia, S. Mukerjee, R. Yang, Z. Jiang, D. Su, C. Liu, W. Xing, *ACS Catal.*, 8 (2018) 2824.
49. X. Yan, Z. Meng, H. Xu, T. Xue, G. Fang, Z. Hu, *Int. J. Electrochem. Sci.*, 14 (2019) 6938.